Journal of Computational Physics 229 (2010) 5921–5932

Contents lists available at ScienceDirect

Journal of Computational Physics

journal homepage: www.elsevier.com/locate/jcp

Generalization of the FDTD algorithm for simulations of hydrodynamic nonlinear Drude model

Jinjie Liu [a,*], Moysey Brio [a], Yong Zeng [a], Armis R. Zakharian [c], Walter Hoyer [b], Stephan W. Koch [b], Jerome V. Moloney [a]

[a] Arizona Center for Mathematical Sciences at Department of Mathematics, University of Arizona, Tucson, AZ 85721, USA
[b] Department of Physics and Material Sciences Center, Philipps University, Renthof 5, D-35032 Marburg, Germany
[c] Corning Inc., One Science Center Dr., SP TD 01-1, Corning, NY 14831, USA

ARTICLE INFO

Article history:
Received 9 March 2009
Received in revised form 3 February 2010
Accepted 9 April 2010
Available online 21 May 2010

Keywords:
Maxwell's equations
FDTD method
Cold-plasma equations
Metamaterials
Second-harmonic generation

ABSTRACT

In this paper we present a numerical method for solving a three-dimensional cold-plasma system that describes electron gas dynamics driven by an external electromagnetic wave excitation. The nonlinear Drude dispersion model is derived from the cold-plasma fluid equations and is coupled to the Maxwell's field equations. The Finite-Difference Time-Domain (FDTD) method is applied for solving the Maxwell's equations in conjunction with the time-split semi-implicit numerical method for the nonlinear dispersion and a physics based treatment of the discontinuity of the electric field component normal to the dielectric-metal interface. The application of the proposed algorithm is illustrated by modeling light pulse propagation and second-harmonic generation (SHG) in metallic metamaterials (MMs), showing good agreement between computed and published experimental results.

1. Introduction

The cold-plasma equations are fundamental hydrodynamic transport equations that describe the mass and momentum conservation of the plasma under the excitation by an external electromagnetic wave governed by the Maxwell's equations [1]. This model has been successfully applied to study electromagnetic wave propagation in plasmas. Recently, a classical theory based on the cold-plasma equations was developed to study the nonlinear optical response from metallic metamaterials (MMs) consisting of periodic arrays of metallic nanostructures [2]. The electrons inside the metal can be approximated as continuous electron gas, and the external electromagnetic wave is governed by the Maxwell's equations. This work was motivated by recent experiments of second-harmonic generation (SHG) from metallic MMs [3–6]. The SHG has been found to be the strongest when the non-centro-symmetric U-shaped metallic split-ring resonators (SSRs) were excited resonantly [4], in comparison to other structures, such as T-shaped and rectangular metal pieces. For centro-symmetric structure such as an array of metallic rectangular sections, the detected second-harmonic strength is much smaller (less than 1%) than that from U shapes. In [2,7], numerical simulations were carried out by expanding electric and magnetic fields as well as charge and current densities into first-order linear response and second-order nonlinear response. Numerical results yielded good agreement with experiments and showed that the major contribution source of the SHG is the convective derivative term in the cold-plasma equations. It should be pointed out that the model proposed in [2] focuses on studying

* Corresponding author. Tel.: +1 520 621 6209; fax: +1 520 621 1510.
E-mail addresses: jliu@math.arizona.edu (J. Liu), brio@math.arizona.edu (M. Brio), zengy@acms.arizona.edu (Y. Zeng), zakhariaar@corning.com (A.R. Zakharian), Walter.Hoyer@Physik.Uni-Marburg.de (W. Hoyer), Stephan.W.Koch@Physik.Uni-Marburg.de (S.W. Koch), jml@acms.arizona.edu (J.V. Moloney).

0021-9991/$ - see front matter © 2010 Elsevier Inc. All rights reserved.
doi:10.1016/j.jcp.2010.04.016

the contribution from the metal bulk structure with normally incident light, while the hydrodynamic model developed several decades ago examines the SHG at flat metal surfaces with obliquely incident light [8,9].

The Finite-Difference Time-Domain (FDTD) method (Yee's scheme), that was originally designed for non-dispersive linear dielectric materials, has been successfully and widely used to model electromagnetic waves for more than four decades [10–12]. By using the auxiliary differential equation (ADE) technique, the FDTD method has been extended to model more complicated materials, such as dispersive and nonlinear media. For linear dispersive materials, the electric permittivity $\epsilon(\omega)$ is a function of frequency, and the ADE can be derived by transforming the polarization equation $\mathbf{P} = \epsilon(\omega)\mathbf{E}$ from frequency domain into time domain, for example, the linear Debye, Drude and Lorentz models can be derived using this approach [13]. For nonlinear materials, such as the Kerr and Raman nonlinear dispersive media, the electric permittivity depends on the intensity of the electric field, and appropriate ADE FDTD methods with nonlinear driving terms were developed in [14,15].

In this paper, we show that the model based on the cold-plasma equations, that was proposed in [2], is a generalization of the linear Drude model to the nonlinear case, and thus we refer to this model as nonlinear Drude model. It is based on the classical hydrodynamic theory for electrons. The full coupled fluid-Maxwell system of equations is approximated numerically without the expansion into orders of the exciting electric field as applied in [2]. In our numerical method the nonlinear Drude fluid equations for the current density $\mathbf{J}$ are solved using a time-split semi-implicit finite difference algorithm. A critical issue in the numerical design is a physics based treatment of the discontinuity of the normal electric field component at the dielectric-metal interface. It has been pointed out in [8] that the computation of electron charge density ($\nabla \cdot \mathbf{E}$) at the dielectric-metal interface is ambiguous due to the discontinuity of the normal electric field. To overcome this critical problem, we introduce a transition layer with smoothed ion distribution between metal and the surrounding dielectric media as suggested by the quantum theory. This regularization provides continuous normal electric field so that the computation of $\nabla \cdot \mathbf{E}$ is physical and the singularity is eliminated. To illustrate the performance of the proposed algorithm we applied it to the problem of SHG emitted by a single periodic layer of gold nanostructures on glass. Our numerical simulations in a three-dimensional computational domain yield good agreement with the experimental result in [3,4] and the numerical results based on the asymptotic theory reported in [2].

The paper is organized as follows. In Section 2, we introduce the nonlinear Drude model that describes the motion of the electrons inside the metallic dispersive media. Time-split numerical method for solving the nonlinear Drude fluid model is described in Section 3. In Section 4, we investigate the accuracy of the numerical solution and the resolution requirements resulting from the introduction of the transition layer at the dielectric-metal interface. In Section 5, we present results of the numerical simulations of the optical pulse propagation and SHG in metallic MMs and compare the computed results with the published experimental data.

2. The Nonlinear Drude model

The nonlinear Drude model for modeling nonlinear dispersive media is derived from the cold-plasma equations and is coupled to the Maxwell's field equations [2]. The cold-plasma equations for the electron density n_e and velocity $\mathbf{u}_e$ and the Maxwell's equations for electromagnetic fields $\mathbf{E}$ and $\mathbf{B}$ are given by

$$\frac{\partial n_e}{\partial t} + \nabla \cdot (n_e \mathbf{u}_e) = 0, \tag{1}$$

$$\frac{\partial \mathbf{u}_e}{\partial t} + (\mathbf{u}_e \cdot \nabla)\mathbf{u}_e = \frac{q_e}{m_e}(\mathbf{E} + \mathbf{u}_e \times \mathbf{B}), \tag{2}$$

$$\nabla \cdot \mathbf{B} = 0, \tag{3}$$

$$\epsilon_0 \nabla \cdot \mathbf{E} = \rho, \tag{4}$$

$$\frac{\partial \mathbf{B}}{\partial t} = -\nabla \times \mathbf{E}, \tag{5}$$

$$\epsilon_0 \frac{\partial \mathbf{E}}{\partial t} = \frac{1}{\mu_0}\nabla \times \mathbf{B} - \mathbf{J}, \tag{6}$$

where m_e, q_e, ϵ_0 and μ_0 are the electron mass, electron charge, vacuum permittivity and vacuum permeability, respectively, and the electron number density and velocity field are denoted by $n_e(\mathbf{r})$ and $\mathbf{u}_e(\mathbf{r})$. Eq. (1) is the continuity equation and Eq. (2) is the generalization of the Newton's second law. Eqs. (3)–(6) are the Maxwell's equations. The charge density ρ and the current density $\mathbf{J}$ are defined as

$$\rho = q_e(n_e - n_0), \tag{7}$$

$$\mathbf{J} = q_e n_e \mathbf{u}_e, \tag{8}$$

where n_0 is the positive ion density which is assumed to be constant in time. Initially, before the exciting field comes in, also the electron density is equal to n_0 in order to ensure charge neutrality. By rewriting Eqs. (1) and (2) in terms of the charge density ρ and current density $\mathbf{J}$ using the convective derivative, we obtain

$$\frac{\partial \rho}{\partial t} = -\nabla \cdot \mathbf{J}, \tag{9}$$

$$\frac{\partial \mathbf{J}}{\partial t} + \sum_k \frac{\partial}{\partial x_k}\frac{\mathbf{J}J_k}{q_e n_e} = \frac{q_e}{m_e}(q_e n_e \mathbf{E} + \mathbf{J}\times\mathbf{B}) - \frac{1}{\tau}\mathbf{J}, \tag{10}$$

where τ is the phenomenological damping time constant. The term $\mathbf{J}/\tau$ is added to describe the current decay due to Coulomb scattering. Eq. (9) can be derived from Eq. (6) by taking its divergence. As a result, Eqs. (9) and (10) can be reduced to the following equation

$$\frac{\partial \mathbf{J}}{\partial t} = -\frac{1}{\tau}\mathbf{J} + \epsilon_0\omega_p^2\mathbf{E} + \frac{q_e}{m_e}(\rho\mathbf{E} + \mathbf{J}\times\mathbf{B}) - \sum_k \frac{\partial}{\partial x_k}\left(\frac{\mathbf{J}J_k}{\rho + \epsilon_0 m_e\omega_p^2/q_e}\right), \tag{11}$$

where $\omega_p(\mathbf{r}) = \sqrt{q_e^2 n_0(\mathbf{r})/(\epsilon_0 m_e)}$ is the space-dependent plasma frequency. The last two terms on the right hand side of Eq. (11) introduce the nonlinearity into the system, while the first two correspond to the linear Drude model for dispersive media [13]

$$\frac{\partial \mathbf{J}}{\partial t} = -\frac{1}{\tau}\mathbf{J} + \epsilon_0\omega_p^2\mathbf{E}.$$

3. The Numerical method for nonlinear Drude model

In this section, we present a numerical method for solving the system of Eqs. (5), (6) and (11). The Maxwell equations (5) and (6) are solved using the FDTD method [10,11,13] and the nonlinear Drude equation (11) is solved using a time-split semi-implicit finite difference method. Microscopically, no magnetic resonances exist in our model such that $\mathbf{B} = \mu_0\mathbf{H}$ in the whole paper.

3.1. The computational grids

The computational grid follows the standard staggered Yee mesh. The electric field **E**, magnetic field **H** and current density **J** are staggered both in space and time. The position of **J**s is the same as of **E**s in space and the same as for **H**s in time. The $\nabla\cdot\mathbf{E}$ terms are first calculated at the cell centers and then interpolated to the position where **E**s are defined. When updating **J**, our numerical method requires all components of **J** to be collocated, which is achieved by the interpolation of **J**s to cell centers. A computational cell with lower-left corner (i,j,k) and upper-right corner $(i+1, j+1, k+1)$ is shown in Fig. 1. In this grid cell, **E** components are defined at time level n and are located at the computational cell face centers: $E^n_{x\,i,j+1/2,k+1/2}$, $E^n_{y\,i+1/2,j,k+1/2}$, and $E^n_{z\,i+1/2,j+1/2,k}$; **H** components are defined at time level $n+1/2$ and are located along the edges of the computational cell: $H^{n+1/2}_{x\,i+1/2,j,k}$, $H^{n+1/2}_{y\,i,j+1/2,k}$, and $H^{n+1/2}_{z\,i,j,k+1/2}$; components of **J** are defined at time level $n+1/2$ and are located at the face centers of the computational cell: $J^{n+1/2}_{xi,j+1/2,k+1/2}$, $J^{n+1/2}_{yi+1/2,j,k+1/2}$, and $J^{n+1/2}_{zi+1/2,j+1/2,k}$. The $\nabla\cdot\mathbf{E}^n$ terms are computed at the cell centers as

$$\nabla\cdot\mathbf{E}^n_{i+1/2,j+1/2,k+1/2} = \frac{\Delta E^n_x}{\Delta x} + \frac{\Delta E^n_y}{\Delta y} + \frac{\Delta E^n_z}{\Delta z}, \tag{12}$$

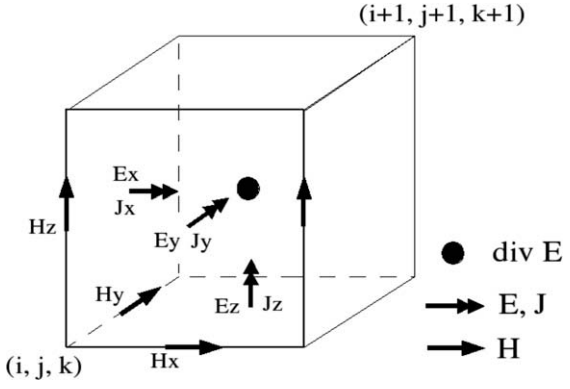

Fig. 1. Positions of the field components in a computational cell.

where

$$\Delta E_x^n = E_{x\,i+1,j+1/2,k+1/2}^n - E_{x\,i,j+1/2,k+1/2}^n,$$
$$\Delta E_y^n = E_{y\,i+1/2,j+1,k+1/2}^n - E_{y\,i+1/2,j,k+1/2}^n,$$
$$\Delta E_z^n = E_{z\,i+1/2,j+1/2,k+1}^n - E_{z\,i+1/2,j+1/2,k}^n.$$

3.2. Numerical discretization of the nonlinear Drude equations

A time-split semi-implicit finite difference method is employed to discretize the nonlinear Drude equation (11) by splitting it into the following three subproblems:

$$\frac{\partial \mathbf{J}}{\partial t} = -\frac{1}{\tau}\mathbf{J} + \epsilon_0\omega_p^2\mathbf{E} + \frac{q_e}{m_e}\epsilon_0(\nabla\cdot\mathbf{E})\mathbf{E}, \tag{13}$$
$$\frac{\partial \mathbf{J}}{\partial t} = \frac{q_e}{m_e}\mathbf{J}\times\mathbf{B}, \tag{14}$$
$$\frac{\partial \mathbf{J}}{\partial t} = -\sum_k \frac{\partial}{\partial x_k}\left(\frac{\mathbf{J}J_k}{\rho + \epsilon_0 m_e\omega_p^2/q_e}\right). \tag{15}$$

The algorithm proceeds as follows. First, using Eq. (13), we update $\mathbf{J}$ from time level $n-1/2$ to $n+1/2$ utilizing an implicit time update with respect to $\mathbf{J}$ and explicit central differencing for other terms. We obtain

$$\frac{\mathbf{J}^{(1)} - \mathbf{J}^{n-1/2}}{\Delta t} = -\frac{\mathbf{J}^{(1)} + \mathbf{J}^{n-1/2}}{2\tau} + \epsilon_0\omega_p^2\mathbf{E}^n + \frac{q_e}{m_e}\epsilon_0(\nabla\cdot\mathbf{E}^n)\mathbf{E}^n, \tag{16}$$

where $\mathbf{J}^{(1)}$ is the intermediate updated value of $\mathbf{J}$ at time level $n+1/2$. The $\nabla\cdot\mathbf{E}^n$ term is evaluated as described in Eq. (12). Since it is needed at the same grid positions as the electric field, the divergence is interpolated. For example, for the x-component of $\mathbf{E}$, defined at $(i, j+1/2, k+1/2)$, we have

$$\nabla\cdot\mathbf{E}_{i,j+1/2,k+1/2}^n = \frac{1}{2}\left(\nabla\cdot\mathbf{E}_{i+1/2,j+1/2,k+1/2}^n + \nabla\cdot\mathbf{E}_{i-1/2,j+1/2,k+1/2}^n\right).$$

Eq. (16) can be solved explicitly for updating $\mathbf{J}^{(1)}$,

$$\mathbf{J}^{(1)} = \frac{\tau - \frac{\Delta t}{2}}{\tau + \frac{\Delta t}{2}}\mathbf{J}^{n-1/2} + \frac{\tau\Delta t}{\tau + \frac{\Delta t}{2}}\epsilon_0\left(\omega_p^2\mathbf{E}^n + \frac{q_e}{m_e}(\nabla\cdot\mathbf{E}^n)\mathbf{E}^n\right). \tag{17}$$

Second, we apply an implicit scheme to solve the second Eq. (14). Before updating this equation, we interpolate components of $\mathbf{J}$ to the cell centers. Similarly, $\mathbf{H}$ is interpolated to cell center in space, and also in time to time level n. For example, at cell center $(i+1/2, j+1/2, k+1/2)$, $\widehat{H}_x^n$ and $\widehat{J}_x$ are interpolated using arithmetic averaging as follows,

$$\widehat{J}_x = \frac{1}{2}\left(J_{x\,i,j+1/2,k+1/2}^{(1)} + J_{x\,i+1,j+1/2,k+1/2}^{(1)}\right),$$
$$\widehat{H}_x^n = \frac{1}{2}\left(\widehat{H}_x^{n+1/2} + \widehat{H}_x^{n-1/2}\right),$$
$$\widehat{H}_x^p = \frac{1}{4}\left(H_{x\,i+1/2,j,k}^p + H_{x\,i+1/2,j+1,k}^p + H_{x\,i+1/2,j,k+1}^p + H_{x\,i+1/2,j+1,k+1}^p\right),$$

where $p = n \pm 1/2$ and $J^{(1)}$ is the solution obtained from the previous step of updating Eq. (13). The advantage of collocating $\mathbf{J}$s and $\mathbf{H}$s is that it avoids solving a large matrix system. The resulting implicit method requires a solution to the following 3×3 linear system at each cell center:

$$\frac{\mathbf{J}^{(2)} - \widehat{\mathbf{J}}}{\Delta t} = \frac{q_e}{m_e}\mu_0\frac{\mathbf{J}^{(2)} + \widehat{\mathbf{J}}}{2}\times\widehat{\mathbf{H}}^n, \tag{18}$$

or in matrix form:

$$A\mathbf{J}^{(2)} = A'\widehat{\mathbf{J}}, \tag{19}$$

where

$$A = \begin{pmatrix} 1 & -aH_z & aH_y \\ aH_z & 1 & -aH_x \\ -aH_y & aH_x & 1 \end{pmatrix},$$

A' represents the transpose of A, $\widehat{\mathbf{H}}^n = (H_x, H_y, H_z)'$ and $a = \frac{1}{2}\Delta t\mu_0 q_e/m_e$. The explicit solution of Eq. (19) is

$$\begin{aligned}\mathbf{J}^{(2)} &= A^{-1}A'\widehat{\mathbf{J}} \\ &= \frac{1}{|A|}\begin{pmatrix} 1+a^2(H_x^2-H_y^2-H_z^2) & 2a(aH_xH_y+H_z) & 2a(aH_zH_x-H_y) \\ 2a(aH_xH_y-H_z) & 1+a^2(H_y^2-H_z^2-H_x^2) & 2a(aH_yH_z+H_x) \\ 2a(aH_zH_x+H_y) & 2a(aH_yH_z-H_x) & 1+a^2(H_z^2-H_x^2-H_y^2) \end{pmatrix}\widehat{\mathbf{J}},\end{aligned} \tag{20}$$

where $|A| = 1 + a^2(H_x^2 + H_y^2 + H_z^2)$.

The final step is to update Eq. (15), which can be written as nonlinear hyperbolic system in conservation form

$$\frac{\partial \mathbf{J}}{\partial t} + (F(\mathbf{J}))_x + (G(\mathbf{J}))_y + (K(\mathbf{J}))_z = 0, \tag{21}$$

where $F(\mathbf{J}) = \mathbf{J}\,J_x/\rho'$, $G(\mathbf{J}) = \mathbf{J}\,J_y/\rho'$, $K(\mathbf{J}) = \mathbf{J}\,J_z/\rho'$, and $\rho' = \rho + \epsilon_0 m_e \omega_p^2/q_e$. Eq. (21) is a system of hyperbolic equations [16], and we apply a two-step Lax–Wendroff scheme [17] to solve it. The time step is chosen to satisfy the CFL conditions for both the hyperbolic system (15) and the Maxwell's equations (with an additional factor of 2) as $\Delta t < \Delta x/(2 \max(V_{max}, c))$, where c is the speed of light in vacuum and $V_{max} = max|\mathbf{J}/\rho'|$ is the maximum wave speed in the plasma. After Eq. (15) has been updated, all components of the current density J are interpolated back to their original locations at the cell face centers and are ready to be used by the FDTD method for updating the **E** field. The linear time-splitting in this implementation results in a first order scheme. The three-step splitting scheme is chosen for simplicity and efficiency of the implementation. In particular, we obtain a small 3×3 system instead of a large matrix equation involving the whole system. The computation of a local 3×3 system is explicit and is much cheaper than the solution of a large matrix of the size of the whole computational domain times the number of variables involved, three *E*s, three *B*s and three *J*s. The stability of the Maxwell equations as of any hyperbolic system is not affected by lower order terms or sources as long as the evolution of sources is done stably itself [18,19]. The Yee scheme preserves the divergence free condition (3) for any J (x,t) due to preservation of $\nabla \times (\nabla\phi) = 0$ and $\nabla \cdot (\nabla \times v) = 0$ (ϕ is a scalar and v is a vector) for discrete approximations of these differential operator.

4. Regularization of dielectric-metal interface

At the dielectric-metal interface the normal components of the electric field and the current density are discontinuous. As a result, the computation of electron charge density ($\nabla \cdot \mathbf{E}$) at the dielectric-metal interface is ambiguous. For example, evaluating $\nabla \cdot \mathbf{E}$ using the fields on both sides of the interface on a given mesh in most cases will produce non-physical results. Therefore, when the nonlinear Drude model is applied to media with the dielectric/nonlinear dispersive material interfaces, the computation of the electric charge requires a regularization procedure. In particular, a metal-vacuum selvedge method [8] and a smooth Jellium model [20,9] were proposed for the metal-vacuum interface regularizations based on the quantum theory. The metal-vacuum selvedge method introduced a selvedge region between the metal and vacuum with the effective current density in the selvedge treated as a delta function. In the Jellium model, the ion density n_0 varies from its bulk value to zero over a short distance on the order of the Fermi wavelength [20]. The works presented in [8,20,9] were designed for flat metal surfaces. Recently, this model has been extended to non-flat periodically-structured metal surfaces with application in studying SHG [21]. The method presented in [21] is based on the analytic parametrizations of the SHG and can be solved either analytically or numerically by the FDTD method. Notice that these models are based on the parametrizations of the SHG, which is different from our work based on solving numerically the full cold-plasma Maxwell system.

In this paper, we apply a smooth transition layer between the metal and dielectric materials. Similar to the previously proposed Jellium model, we allow the ion density to vary from its bulk value to zero smoothly within the transition layer. Assuming the dielectric-metal interface is normal to the x-direction and the transition layer interval is of fixed width, $x \in (-1, 1)$. $n_0(x)$ is given by the following function:

$$n_0(x) = \begin{cases} n_{bulk} & x \leqslant -1, \\ f(x) \cdot n_{bulk} & -1 < x < 1, \\ 0 & x \geqslant 1, \end{cases} \tag{22}$$

where $n_0(x)$ is the ion density near the dielectric-metal interface, $n_{bulk} = \omega_p^2 \epsilon_0 m_e/q_e^2$ is the bulk ion density in the metal and $f(x)$ gives the ion distribution in the transition layer. A simple choice of $f(x)$ is a linear polynomial $f(x) = \frac{1}{2}(1 - x)$.

We test our approach by studying the transmission of an optical pulse through thin metal layers. The simulated metallic structures are rectangular or L-shaped in the $x - y$ plane, infinitely long in the z-direction. In addition, the structure is periodically replicated in the x-direction. The dimensions of the metal structures are shown in Fig. 2. The metal is modeled using the nonlinear Drude model with plasma frequency $\omega_p = 1.367 \times 10^{16}\ s^{-1}$ and phenomenological damping time constant $\tau = 15.44$ fs, see [22]. The rest of the computational domain is vacuum. The incident light is a z-polarized Gaussian pulse with carrier wavelength $\lambda = 1200$ nm, peak amplitude $E_0 = 2 \times 10^7$ V/m, propagating along the y-direction. The light source is generated by total-field/scattered-field (TFSF) method [13]. Periodic boundaries are used in the x-direction and the perfectly matched layer absorbing (PML) boundaries [23,13] are applied in the y-direction.

Fig. 3 shows the regularized ion distribution near the L-shaped nanostructure, in comparison with the non-regularized results. The transition layer allows the ion density n_0 to decay from its bulk value in the metal to zero in dielectric medium.

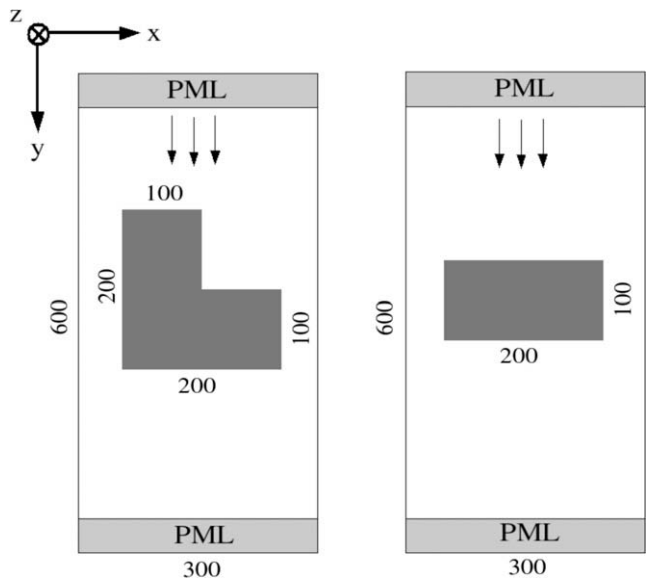

Fig. 2. Two-dimensional computational domain for SHG problem for (a) L-shaped, (b) rectangular gold nanostructures. The units shown are in nm.

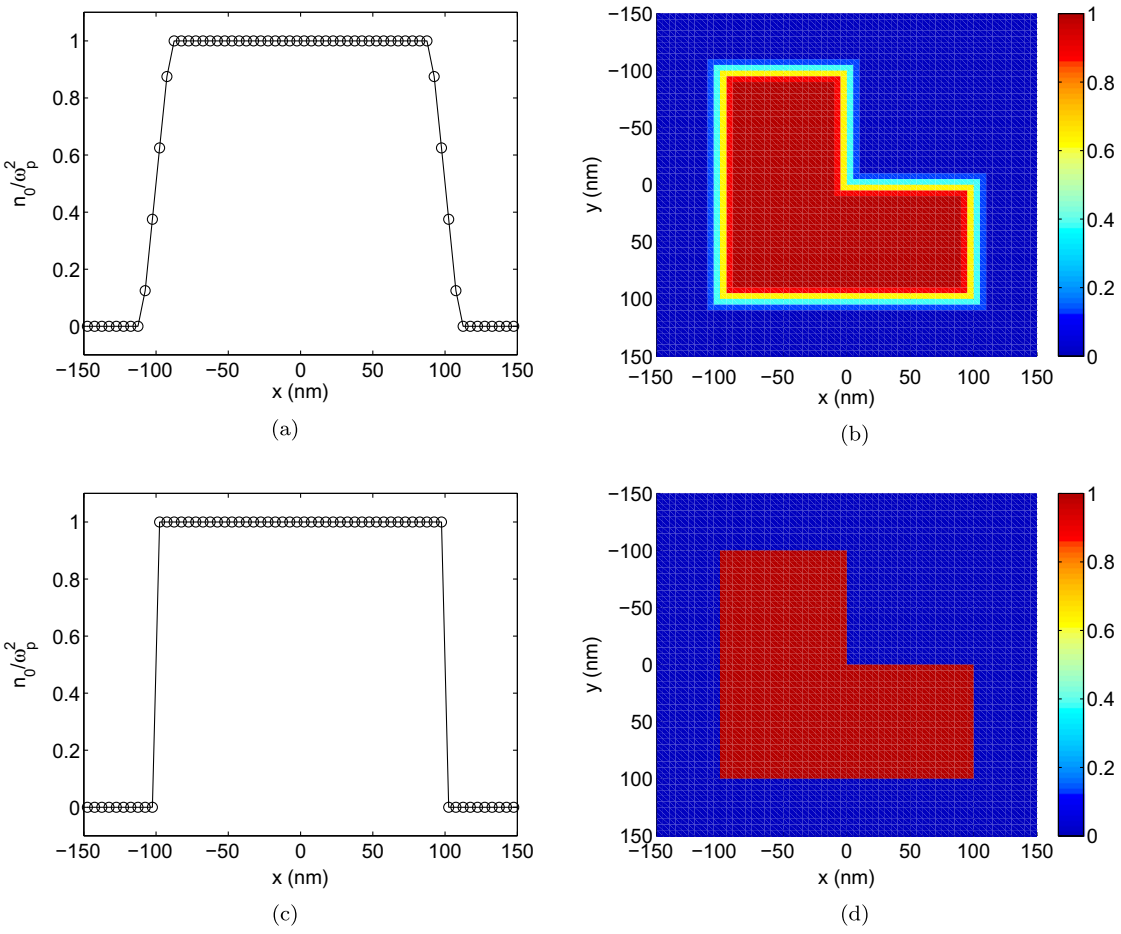

Fig. 3. One dimensional cuts along the x-axis at $y = 50$ nm for (a) regularized, (c) non-regularized relative ion distribution n_0/ω_p^2 near the L-shaped metallic nanostructure. The corresponding contour plots are shown in (b) and (d), respectively.

With this regularization, as shown in Figs. 4 and 5, the normal electric field and normal current density are smoothed, thus regularizing the computation of the charge density $\rho = \epsilon_0 \nabla \cdot \mathbf{E}$. Notice that the non-regularized normal electric field has sharp discontinuity at the dielectric-metal interface, so the numerical computation of the $\nabla \cdot \mathbf{E}$ is proportional to $1/\Delta x$, which will eventually go to positive or negative infinity.

To characterize the linear response and the second-harmonic signal we compute the E_z and E_x components of the transmitted electric field. We measure the transmission of the linear response showing the E_z component of the electric field and for the second-harmonic signal we provide the E_x. For rectangular shape, our numerical result shows no SHG, which is in agreement with the known fact that the centro-symmetry of the structure prohibits the SHG. Fig. 6 shows the time history (in time domain and in frequency domain) of the incident pulse, linear and nonlinear responses for the L-shaped MMs. In Fig. 6(d), both the second-harmonic wave (at wavelength 600 nm) and the third-harmonic wave (at wavelength 400 nm) are detected.

The thickness of the transition layer, as suggested by Drude, should equal to the lattice constant of the metal crystal [24]. For gold it is about 0.32 nm. To resolve this layer in our finite-difference simulation, the grid size therefore cannot be bigger than 0.16 nm, that is, half of the layer thickness. This fine mesh requires a computational burden far beyond our current capacity. The smallest grid cell we can afford is 0.5 nm, we therefore set the transition layer thickness to at least 1 nm. To study its influence, we have fixed the grid size ($\Delta x = \Delta y = \Delta = 0.5$ nm) and varied the transition layer thickness from 10 nm to 1 nm, keeping it resolved with at least two grid-points for the narrowest case. As shown in Fig. 7(a), as the transition layer thickness decreases from 10 nm to 1 nm, the SHG strength decreases continuously. It is also shown that the case of a 5 nm transition layer already provides an acceptable accuracy. With the transition layer thickness fixed at 10 nm, in Fig. 7(b) we show the convergence of the amplitude of the second-harmonic signal as the mesh size tends to zero. The finest grid result with $\Delta = 0.5$ nm and 10 nm thick transition layer is used as the reference solution. For a 10 nm thick transition layer, the simulation with a cell size of 5 nm (1/2 of the transition layer) provides a reasonable result within 80% of the ref-

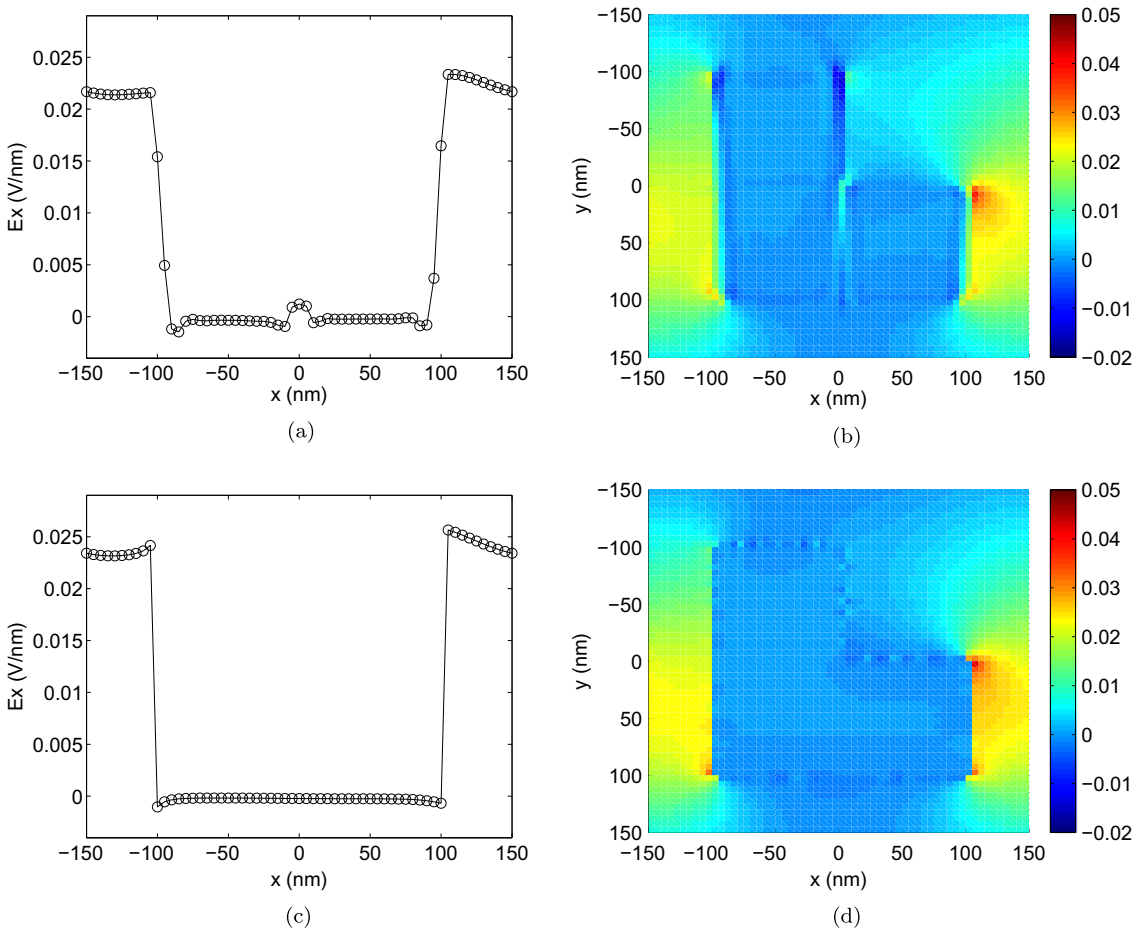

Fig. 4. One dimensional cuts along the x-axis at $y = 50$ nm for (a) regularized, (c) non-regularized normal electric field component E_x near the L-shaped metallic nanostructure. The corresponding contour plots are shown in (b) and (d), respectively.

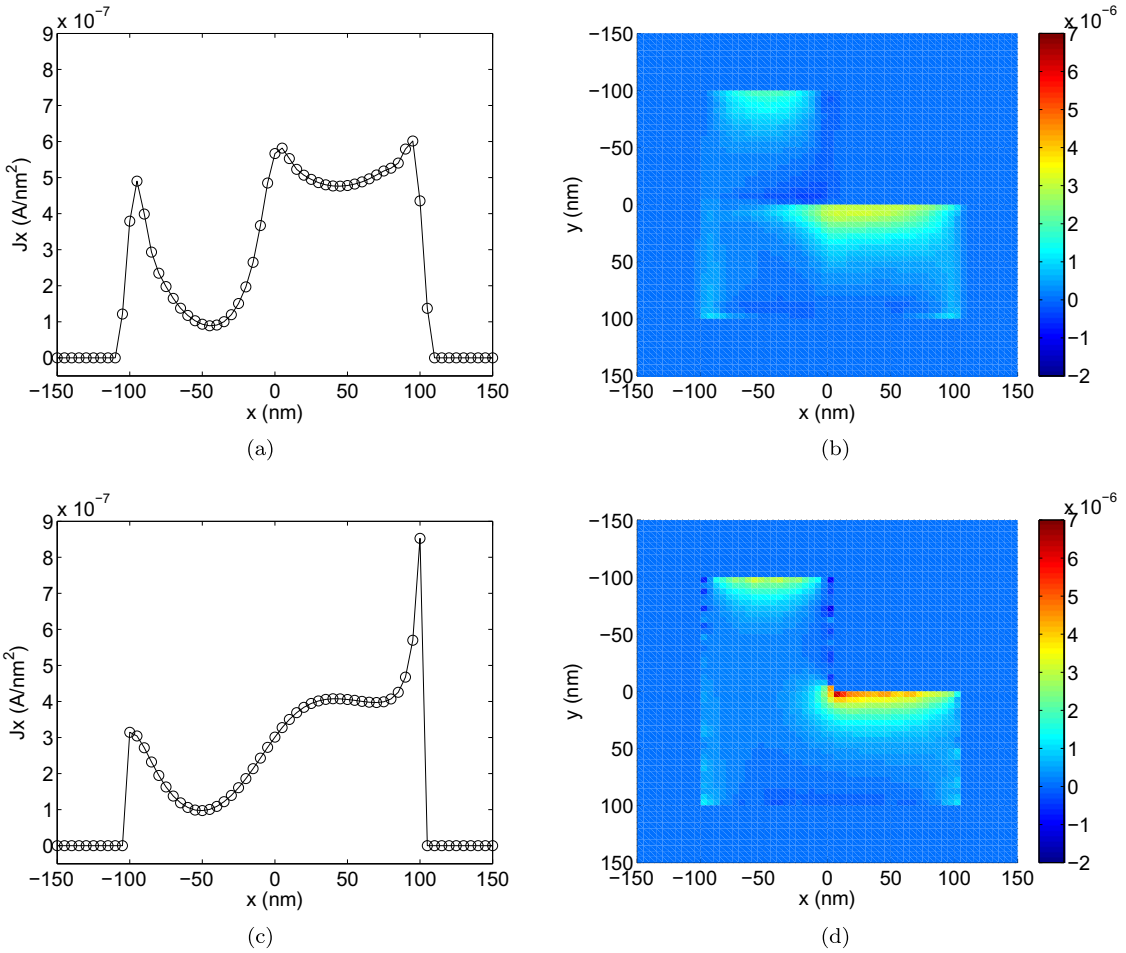

Fig. 5. One dimensional cuts along the x-axis at $y = 50$ nm for (a) regularized, (c) non-regularized normal current density J_x near the L-shaped metallic nanostructure. The corresponding contour plots are shown in (b) and (d), respectively.

erence case, while the cell size of 2 nm (1/5 of the transition layer) leads to the answer within 90% of the reference solution. The extrapolated value at $\Delta x = 0$ nm is 0.01, which provides a solution within 98% accuracy.

5. Numerical simulation of SHG from metallic metamaterials

In this section, we study the SHG from metallic MMs and compare our numerical results with physical experiments presented in [3,4]. The three-dimensional computational domain shown in Fig. 8(a) has periodic boundaries in x- and y-directions and perfectly matched layer (PML) absorbing boundaries in the z-direction. The gold nanostructures are arranged periodically in the x–y plane and they are supported by glass substrate coated with a thin film of indium-tin-oxide (ITO) [3]. The thickness of the gold structures and the ITO layer are 25 nm and 5 nm, respectively. The ITO layer and the glass substrate are dielectric materials and their relative permittivities are 3.8 and 2.25, respectively. The incident Gaussian pulse is x- or y-polarized and propagates along the z-direction. The carrier wavelength and amplitude are $\lambda = 1500$ nm and $E_0 = 2 \times 10^7$ V/m, respectively. The x–y cross sections of the modeled U-shaped, T-shaped and rectangular gold nanostructures are shown in Fig. 8(b). The parameters of gold are the same as in the previous section ($\omega_p = 1.367 \times 10^{16}$ s^{-1} and $\tau = 15.44$ fs).

In our simulations we used a uniform grid with $\Delta x = \Delta y = \Delta z = 2.5$ nm. To speed up the turn around time due to computational intensity of the model, we have used a 10 nm thick transition layer. Fig. 9 shows the time history (in time domain and in frequency domain) of the incident pulse, linear and nonlinear responses for the U-shaped MMs by x-polarized incident pulse. The results of our computation are summarized in Table 1 in terms of the energy conversion efficiency of SHG defined as

$$\eta_2 = \sqrt{\epsilon_{glass}} \left| \frac{E_2(2\omega)}{E_i(\omega)} \right|^2,$$

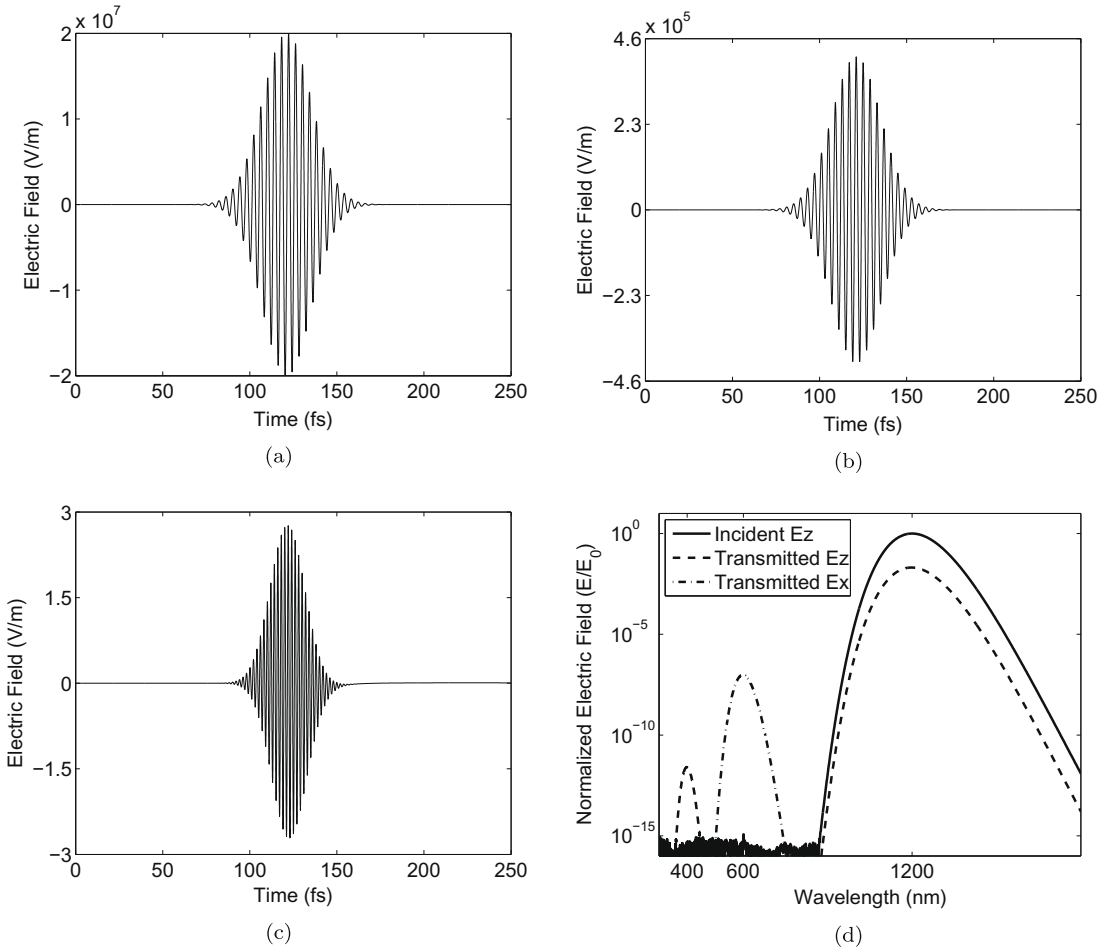

Fig. 6. Time history of (a) the incident pulse, (b) the linear response, (c) the second-harmonic signal amplitude for L-shaped MMs illuminated by a z-polarized incident light. (d) Semi-log plot of the Fourier transform of the time history of the far-field projection of the E_x and E_z components of the electric field as functions of the wavelength with a logarithmic scale on the y-axis and a linear scale on the x-axis.

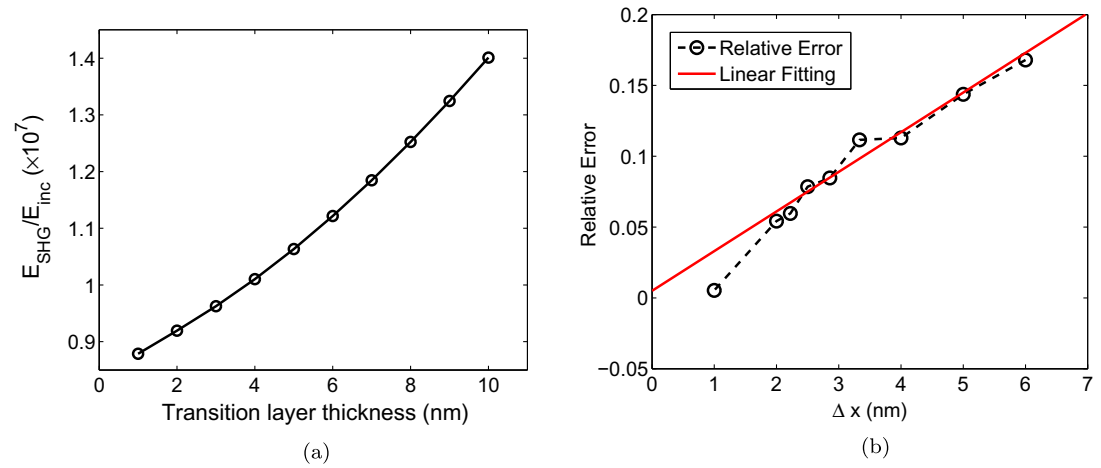

Fig. 7. (a) Normalized SHG signal strength as a function of the transition layer thickness, computed with Δx fixed at 0.5 nm; (b) relative error in SHG signal strength vs the grid step size, computed with the transition layer thickness fixed at 10 nm.

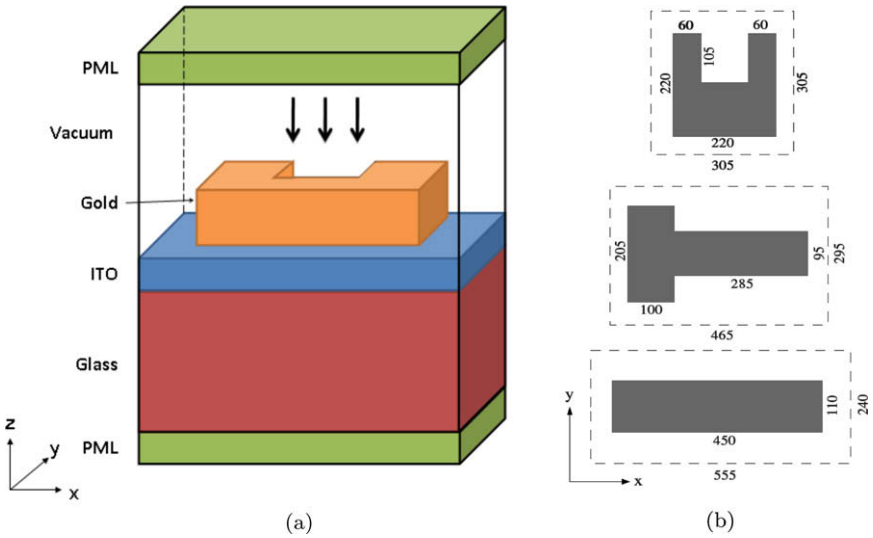

Fig. 8. (a) The computational domain for light pulse propagation through three dimensional gold nanostructures with ITO and glass substrates; (b) $x-y$ cross-sections of U-shaped, T-shaped and rectangular gold nanostructures (units shown in nm).

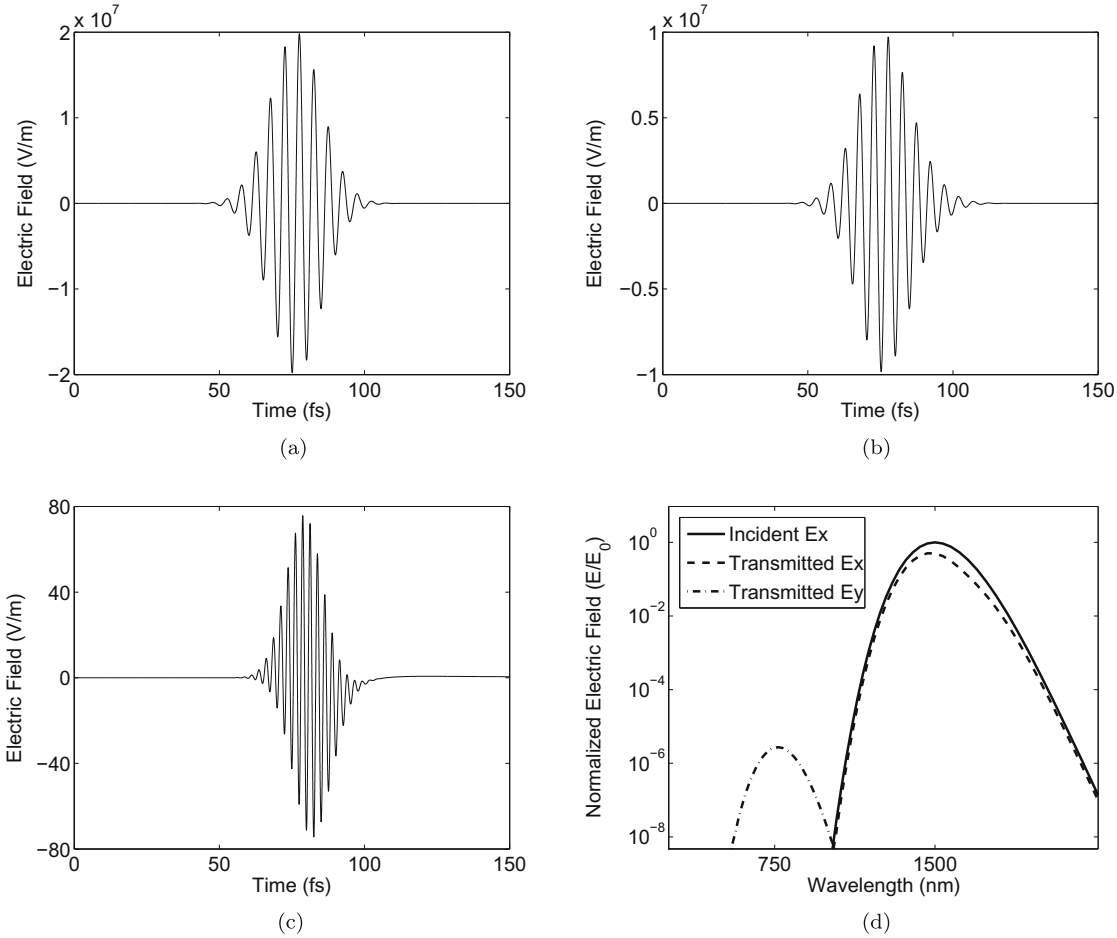

Fig. 9. Time history of (a) the incident pulse, (b) the linear response, (c) the second-harmonic signal for U-shaped MMs by x-polarized incident light. (d) Log-log plot of the Fourier transform of the time history of the far-field projection of the E_x and E_y components of the electric field as functions of the wavelength.

Table 1
Comparison between experimental and numerical results on SHG conversion efficiency. The signal for U-shaped structure and *x*-polarized incident light is normalized to 100%, and all other signals are related to this value.

MMs	Polarization		SHG Conversion Efficiency	
	Incident	SH	Experimental	Numerical
U	*x*	*y*	2×10^{-11}(100%)	1.05×10^{-11}(100%)
U	*y*	*y*	1%	2.1%
T	*x*	*x*	1%	1.8%
rectangle	*x*	*y*	1%	0

where E_i is the incident pulse amplitude, E_2 is the second-harmonic signal. The $\sqrt{\epsilon_{glass}}$ is added to account for the fact that the second-harmonic wave is measured inside the infinite-thick glass substrate [25]. We have normalized the SHG signals for U-shaped structures illuminated by the *x*-polarized incident light to 100% and relate all others to this value. For U-shaped MMs illuminated by *x*-polarized incident light, the SHG conversion efficiency computed by our model is 1.0×10^{-11}, which is close to the experimental results ($\sim 2.0 \times 10^{-11}$) and the calculated value in [2] (6.7×10^{-11}). The experimental results (Table 1) are taken from [3–5]. Notice that the absolute value of SHG conversion efficiency reported in [4] has been corrected in the erratum [5]. Our numerical results on the SHG for other structures also yield good agreement with experiments.

6. Conclusion

We have presented a time-split numerical method for solving the cold-plasma Maxwell system. The cold-plasma equations for modeling hydrodynamic nonlinear dispersive Drude media were coupled in a stable and accurate algorithm to the standard FDTD method for the Maxwell's equations. We have also successfully introduced a transition layer technique that addresses the critical issue of the physical treatment of the discontinuity of the normal electric field component at the dielectric-metal interface. The application of the newly proposed method was illustrated by modeling light propagation in complex media to study the second-harmonic generation (SHG) from metallic metamaterials (MMs) and have yielded a good agreement with experiments.

Acknowledgments

The authors thank Dr. Jörg Hader and Dr. Miroslav Kolesik for helpful discussions. This work was supported by the Air Force Office of Scientific Research (AFOSR) under Grant Nos. FA9550–07-1–0010 and FA9550–04-1–0213. Moysey Brio also would like to acknowledge the support from NSF Grant ITR-0325097.

References

[1] J.A. Bittencourt, Fundamentals of Plasma Physics, third ed., Springer, 2004.
[2] Y. Zeng, W. Hoyer, J. Liu, S.W. Koch, J.V. Moloney, A classical theory for second-harmonic generation from metallic nanoparticles, Phys. Rev. B 79 (2009) 235109.
[3] M.W. Klein, C. Enkrich, M. Wegener, S. Linden, Second-harmonic generation from magnetic metamaterials, Science 313 (2006) 502–504.
[4] M.W. Klein, M. Wegener, N. Feth, S. Linden, Experiments on second- and third-harmonic generation from magnetic metamaterials, Opt. Express 15 (8) (2007) 5238–5247.
[5] M.W. Klein, M. Wegener, N. Feth, S. Linden, Experiments on second- and third-harmonic generation from magnetic metamaterials: erratum, Opt. Express 16 (2008) 8055.
[6] B.K. Canfield, H. Husu, J. Laukkanen, B. Bai, M. Kuittinen, J. Turunen, M. Kauranen, Local field asymmetry drives second-harmonic generation in noncentrosymmetric nanodimers, Nano Lett. 7 (5) (2007) 1251–1255.
[7] N. Feth, S. Linden, M.W. Klein, M. Decker, F.B.P. Niesler, Y. Zeng, W. Hoyer, J. Liu, S.W. Koch, J.V. Moloney, M. Wegener, Second-harmonic generation from complementary split-ring resonators, Opt. Lett. 33 (2008) 1975–1977.
[8] J.E. Sipe, V.C.Y. So, M. Fukui, G.I. Stegeman, Analysis of second-harmonic generation at metal surfaces, Phys. Rev. B 21 (1980) 4389–4402.
[9] M. Corvi, W.L. Schaich, Hydrodynamic-model calculation of second-harmonic generation at a metal surface, Phys. Rev. B 33 (6) (1986) 3688–3695.
[10] K.S. Yee, Numerical solution of initial boundary value problems involving Maxwell's equations in isotropic media, IEEE Trans. Antennas Propag. 14 (1966) 302–307.
[11] A. Taflove, M.E. Brodwin, Numerical solution of steady-state electromagnetic scattering problems using the time-dependent Maxwell's equations, IEEE Trans. Microwave Theory Tech. 23 (1975) 623–630.
[12] A. Taflove, A perspective on the 40-year history of FDTD computational electrodynamics, J. Appl. Comput. Electromagn. Soc. 22 (2007) 1–21.
[13] A. Taflove, S. Hagness, Computational Electrodynamics: The Finite-Difference Time-Domain Method, third ed., Artech House, Norwood, MA, 2005.
[14] M. Fujii, M. Tahara, I. Sakagami, W. Freude, P. Russer, High-order FDTD and auxiliary differential equation formulation of optical pulse propagation in two-dimensional Kerr and Raman nonlinear dispersive media, IEEE J. Quantum Electron. 40 (2) (2004) 175–182.
[15] J.H. Greene, A. Taflove, General vector auxiliary differential equation finite-difference time-domain method for nonlinear optics, Opt. Express 14 (18) (2006) 8305–8310.
[16] R. LeVeque, Numerical Methods for Conservation Laws, Birkhäuser Verlag, Basel, Boston, Berlin, 1992.
[17] G. Zwas, On two step Lax–Wendroff methods in several dimensions, Numer. Math. 20 (1973) 350–355.
[18] J. Strikwerda, Finite Difference Schemes and Partial Differential Equations, SIAM, 2004.
[19] B. Gustafsson, H.-O. Kreiss, J. Oliger, Time Dependent Problems and Difference Methods, Wiley, 1995.
[20] J.E. Sipe, G.I. Stegeman, Nonlinear optical response of metal surfaces, in: D. Mills, V. Agranovich (Eds.), Surface polaritons, 1982, pp. 661–701.
[21] W.L. Schaich, Second-harmonic generation by periodically-structured metal surfaces, Phys. Rev. B 78 (2008) 195416.

[22] C. Enkrich, M. Wegener, S. Linden, S. Burger, L. Zschiedrich, F. Schmidt, J. Zhou, T. Koschny, C.M. Soukoulis, Magnetic metamaterials at telecommunication and visible frequencies, Phys. Rev. Lett. 95 (2005) 203901.
[23] J.P. Berenger, A perfectly matched layer for the absorption of electromagnetic waves, J. Comput. Phys. 114 (2) (1994) 185–200.
[24] P. Drude, The Theory of Optics, Longmans, Green and Co., 1902.
[25] R.W. Boyd, Nonlinear Optics, second ed., Academic press, 2003.